Arbitrary-Order Conservative and Consistent Remapping and a Theory of Linear Maps, Part 2

Paul A. Ullrich*

Department of Land, Air and Water Resources, University of California, Davis, California

Dharshi Devendran and Hans Johansen

Lawrence Berkeley National Laboratory, Berkeley, California

**Corresponding author address:* Paul Ullrich, Department of Land, Air and Water Resources, University of California, Davis, 1 Shields Avenue, Davis, California 95616.

E-mail: paullrich@ucdavis.edu

ABSTRACT

This paper extends on the first part of this series by describing four examples of 2D linear maps that can be constructed in accordance with the theory of the earlier work. The focus is again on spherical geometry, although these techniques can be readily extended to arbitrary manifolds. The four maps that are studied include arbitrary-order conservative and consistent (and optionally monotone) linear maps (a) between two finite volume meshes, (b) from finite volume to finite element meshes using a projection-type approach, (c) from finite volume to finite element meshes using volumetric integration and (d) between two finite element meshes.

1. Introduction

This paper follows the earlier work on consistent, conservative and monotone linear maps by Ullrich and Taylor (2015). These maps are built so as to satisfy the linear remapping problem: Given source mesh $\mathscr{F}^s$, target mesh $\mathscr{F}^t$ and vectorized source mesh density field ψ^s, define a matrix operator $\mathbf{R}$ so that

$$\psi^t = \mathbf{R}\psi^s \tag{1}$$

is an accurate representation of the vectorized density field on the target mesh. The first paper in this series described the mathematical properties required of the linear mapping operator for the preservation of these three properties and provided an example of how one could use these properties to construct a high-order linear map from a finite element mesh to finite volume mesh.

This paper extends on this previous work to describe four new examples of techniques for building linear maps. In the process of developing these algorithms, a number of theoretical results are proven to validate that each map satisfies the desired properties of conservation and consistency. The use of the overset grid is again key in the development of these new maps (this concept is closely associated with the supermesh of Farrell et al. (2009) and the notion of common refinement from Jiao and Heath (2004)). It is assumed that the overset mesh is provided, and we refer to either Ullrich and Taylor (2015) or Farrell et al. (2009) for two potential algorithms for its construction.

In section 3, the generation of arbitrary-order finite volume to finite volume maps using an overset mesh generation technique is discussed. In sections 4 and 5 we present two techniques for the generation of maps from finite volumes to finite elements. Finally, in section 6 we discuss the generation of maps from finite elements to finite elements via Galerkin projection when exact integration is unavailable.

2. Preliminaries

The four meshes used in this paper are depicted in Figure 1. These include (a) the cubed-sphere, (b) the great-circle regular-latitude-longitude meshes, (c) the tessellated cubed-sphere mesh, and (d) the icosahedral flag grid. The first two of these are also used in Ullrich and Taylor (2015). The tessellated cubed-sphere is generated by inserting nodes at the center of each cubed-sphere face and then building new quadrilateral faces around each edge (Weller 2013). The icosahedral flag grid is generated by regularly sub-dividing faces of the icosahedron into sub-triangles and then further sub-dividing each triangle into three quadrilaterals (Giraldo 2001). Meshes (a), (c) and (d) have been constructed using the SQuadGen spherical quadrilateral mesh generation utility (`http://climate.ucdavis.edu/squadgen.php`) (Guba et al. 2014).

Following Ullrich and Taylor (2015), standard error measures are employed:

$$L_1 \equiv \frac{I^t\left[\left|\mathbf{R}\mathbf{D}^s[\psi] - \mathbf{D}^t[\psi]\right|\right]}{I^t\left[\left|\mathbf{D}^t[\psi]\right|\right]}, \qquad L_2 \equiv \frac{\sqrt{I^t\left[\left|\mathbf{R}\mathbf{D}^s[\psi] - \mathbf{D}^t[\psi]\right|^2\right]}}{\sqrt{I\left[\left|\mathbf{D}^t[\psi]\right|^2\right]}}, \tag{2}$$

$$L_\infty \equiv \frac{\max\left|\mathbf{R}\mathbf{D}^s[\psi] - \mathbf{D}^t[\psi]\right|}{\max\left|\mathbf{D}^t[\psi]\right|}, \tag{3}$$

$$L_{min} \equiv \frac{\min\left(\mathbf{D}^t[\psi]\right) - \min\left(\mathbf{R}\mathbf{D}^s[\psi]\right)}{\max\left|\mathbf{D}^t[\psi]\right|}, \qquad L_{max} \equiv \frac{\max\left(\mathbf{R}\mathbf{D}^s[\psi]\right) - \max\left(\mathbf{D}^t[\psi]\right)}{\max\left|\mathbf{D}^t[\psi]\right|} \tag{4}$$

Here $\mathbf{R}$ denotes the linear mapping operator, $\mathbf{D}^s$ and $\mathbf{D}^t$ are discretization operators that take the continuous field ψ to the source and target mesh, and I^t is an integration operator over the target mesh. Validation of the interpolation methodology again uses the three standard fields described in Ullrich and Taylor (2015), including a smoothly varying function Y_2^2, a rapidly varying spherical harmonic Y_{32}^{16} and an artifical vortex.

Throughout this paper geometric consistency is assumed (Ullrich and Taylor 2015, Definition 8). Specifically, this property requires that for each finite element $A \subseteq \{1,\ldots,f^s\}$, the sum of all local weights is consistent with the geometric area. For a discontinuous finite element on the source mesh this requirement can be written as

$$\sum_{k \in A} J_k^s = |\Omega_i^s| \quad (\forall\, i \in A), \tag{5}$$

where J_k^s denotes the weight of degree of freedom k (typically sampled pointwise) and $|\Omega_i^s|$ denotes the geometric area of the degree of freedom i.

3. Finite Volume to Finite Volume Remapping

This section focuses on the development of arbitrary-order conservative and consistent linear maps between arbitrary finite volume (FV) meshes. The basic procedure we propose involves a local reconstruction operation that converts adjacent volume averages into polynomial coefficients, and a second operator that integrates and averages the reconstruction over all target mesh volumes.

Overlapping volumes for FV interpolation have been previously employed by Grandy (1999) in the design of a first-order conservative interpolation scheme. A conservative method using a second-order linear reconstruction was later developed by Garimella et al. (2007). An analogous procedure known as Galerkin projection (Farrell et al. 2009) was also extended by Menon and Schmidt (2011) to finite volume meshes, but again was only assessed for a linear reconstruction. In spherical geometry overlapping volumes were used by Ullrich et al. (2009) for third-order mapping between cubed-sphere and latitude-longitude meshes. Other methods have been developed for spherical geometry that use approximate overlap volumes, such as Jones (1999) and Lauritzen and Nair (2007).

Finite volume maps have largely been pursued in an "online" sense – namely, in the form of an algorithm that transforms source mesh averages to target mesh averages. Linear maps, which are pursued in this paper, can also be applied in an "offline" sense, where the coefficients of the map are stored as a sparse matrix and applied via a computationally efficient and readily parallelized sparse matrix multiply. Previous work by Chesshire and Henshaw (1994) leveraged certain properties of the coefficients of this linear operator to impose conservation on interpolating fluxes for solving PDEs. Nonetheless, to the best of the authors' knowledge, this paper is the first to describe techniques for building arbitrary-order conservative and consistent finite volume maps in arbitrary geometry.

a. Arbitrary-order polynomial reconstruction on a 2D surface

The finite volume reconstruction procedure follows Jalali and Ollivier-Gooch (2013), among others. Consider an arbitrary 2D polygonal face $\mathscr{F}_j^s$ on the source mesh ($j \in \{1,\ldots,f^s\}$) defined by n_j^s 3D corner points $(\mathbf{x}_j^s)_k$, where $k = 1,\ldots,n_j^s$. Corner points are connected by great circle arcs in counter-clockwise order. A polynomial reconstruction is defined via

$$\psi_j^s(\mathbf{x}) = \sum_{p=0}^{p_{max}} \sum_{q=0}^{q_{max}} (c_j^s)^{(p,q)} \alpha(\mathbf{x})^p \beta(\mathbf{x})^q, \tag{6}$$

where α and β are defined implicitly via the unique solution of

$$\begin{aligned} \mathbf{x} &= (\mathbf{x}_j^s)_0 + (\Delta\mathbf{x}_j^s)_\alpha \alpha + (\Delta\mathbf{x}_j^s)_\beta \beta + (\Delta\mathbf{x}_j^s)_\gamma \gamma, \\ (\Delta\mathbf{x}_j^s)_\alpha &= (\mathbf{x}_j^s)_1 - (\mathbf{x}_j^s)_0, \\ (\Delta\mathbf{x}_j^s)_\beta &= (\mathbf{x}_j^s)_2 - (\mathbf{x}_j^s)_0, \\ (\Delta\mathbf{x}_j^s)_\gamma &= (\Delta\mathbf{x}_j^s)_\alpha \times (\Delta\mathbf{x}_j^s)_\beta, \end{aligned} \tag{7}$$

and $(\mathbf{x}_j^s)_0$ is the approximate centroid,

$$(\mathbf{x}_j^s)_0 = \frac{1}{n_j^s} \sum_{k=1}^{n_j^s} (\mathbf{x}_j^s)_k. \tag{8}$$

That is, α and β represent the normalized distance along the vector connecting the approximate centroid to $(\mathbf{x}_j^s)_1$ and $(\mathbf{x}_j^s)_2$ respectively, whereas γ is normalized distance perpendicular to both $(\Delta\mathbf{x}_j^s)_\alpha$ and $(\Delta\mathbf{x}_j^s)_\beta$. This third distance measure is necessary due to the potential curvature of the volumes in 3D and allows for the inversion of the linear system (7). The polynomial reconstruction (6) can be truncated as desired, depending on the preferred character of the reconstruction. We denote the number of coefficients in the truncation by N_c. Two popular truncations of order N_p^s are triangular truncation, defined by $(p_{max} = N_p^s, q_{max} = N_p^s - p, N_c = N_p^s(N_p^s + 1)/2)$, and rectangular truncation, defined by $(p_{max} = N_p^s, q_{max} = N_p^s, N_c = (N_p^s)^2)$. In particular, triangular truncation neglects the tensor product terms in the polynomial expansion which have combined exponent above $N_p^s - 1$. In our experiments, rectangular truncation appears to produce better quality maps when paired with least squares reconstruction, and so it will be employed in the remainder of this manuscript.

The polynomial reconstruction (6) can also be written as the inner product of a position vector $\boldsymbol{\alpha}_j(\mathbf{x}) \in \mathbb{R}^{N_c}$, which is composed of some arrangement of the terms $\alpha(\mathbf{x})^p \beta(\mathbf{x})^q$, and a vector $\mathbf{c}_j \in \mathbb{R}^{N_c}$, composed of the associated reconstruction coefficients c_j^s. The expansion (6) then takes the form

$$\psi_j^s(\mathbf{x}) = \boldsymbol{\alpha}_j(\mathbf{x})^T \mathbf{c}_j. \tag{9}$$

For simplicity, the remainder of this text will assume that the first element of $\boldsymbol{\alpha}_j(\mathbf{x})$ corresponds to the constant mode ($p = q = 0$).

b. Construction of the sub-map

In Ullrich and Taylor (2015), sub-maps were defined as linear operators that map a limited set of degrees of freedom $A \subseteq \{1, \ldots, f^s\}$ from the source mesh to the target mesh. For FV to FV remapping, the sub-map $\hat{\mathbf{R}}^{(j)}$ is constructed for each finite volume $\mathscr{F}_j^s$ and composed via Ullrich and Taylor (2015) Theorem 1. Construction follows a two stage procedure: First, a fit operator $(\mathbf{F}_j^s)^{\oplus} \in \mathbb{R}^{N_c \times f^s}$ is constructed that maps values of the density variable in faces adjacent to $\mathscr{F}_j^s$ to the coefficients of a polynomial expansion. Second, an integration operator $\mathbf{P}_j \in \mathbb{R}^{f^t \times N_c}$ is constructed that maps from the polynomial coefficients to an integrated mass on the target grid. The sub-map is then expressed as

$$\hat{\mathbf{R}}^{(j)} = (\mathsf{diag}\, \mathbf{J}_j^{ov})^{-1} \mathbf{P}_j (\mathbf{F}_j^s)^{\oplus}, \tag{10}$$

where $(\mathsf{diag}\, \mathbf{J}_j^{ov})^{-1} \in \mathbb{R}^{f^t \times f^t}$ is the diagonal matrix whose entries are given by

$$(\mathsf{diag}\, \mathbf{J}_j^{ov})^{-1} = \begin{cases} (J_{i,j}^{ov})^{-1} & \text{if } J_{i,j}^{ov} \neq 0, \\ 0 & \text{otherwise.} \end{cases} \tag{11}$$

In this case, $J_{i,j}^{ov}$ is simply the geometric overlap area between source volume i and target volume j (*i.e.* $J_{i,j}^{ov} = |\Omega_{i,j}^{ov}|$).

c. Building the integration operator

The integration operator $\mathbf{P}_j$ is composed of rows $\mathbf{p}_{i,j}^{ov}$ which represent integration over target volume $i \in \{1, \ldots, f^t\}$ of the reconstruction. Since exact integration may be unavailable, quadrature over triangles is used to define the integration operator, as follows. Each overlap region $\Omega_{i,j}^{ov}$ is decomposed into $N_{i,j}^{ov}$ disjoint triangles in accordance with Ullrich and Taylor (2015) section 3. The set of corner points of each triangular region $n \in \{1, \ldots, N_{i,j}^{ov}\}$ is denoted by $\mathbf{x}_{i,j}^{ov(n)}$, and the area of the triangular region is denoted by $|\Omega_{i,j}^{ov(n)}|$. The integration operator over each overlap region is then constructed by using a triangular quadrature rule ($\hat{w}_q, \hat{\alpha}_q, \hat{\beta}_q$ with $q = 1, \ldots, N_q$) to integrate over the polynomial reconstruction,

$$\mathbf{p}^{ov}_{i,j} = \sum_{n=1}^{N^{ov}_{i,j}} \left| \Omega^{ov(n)}_{i,j} \right| \sum_{q=1}^{N_q} \hat{w}_q \boldsymbol{\alpha}_j(\mathbf{x}_{n,q})^T, \tag{12}$$

$$\text{with} \quad \mathbf{x}_{n,q} = (\mathbf{x}^{ov(n)}_{i,j})_1 \hat{\alpha}_q + (\mathbf{x}^{ov(n)}_{i,j})_2 \hat{\beta}_q + (\mathbf{x}^{ov(n)}_{i,j})_3 (1 - \hat{\alpha}_q - \hat{\beta}_q). \tag{13}$$

Integration and averaging over $\mathscr{F}^s_j$, which will be necessary for verifying conservation, is performed via summation over all target elements, and denoted by

$$\overline{\mathbf{p}}^s_j = \frac{1}{J^s_j} \sum_{i=1}^{f^t} \mathbf{p}^{ov}_{i,j}. \tag{14}$$

With this definition, the following result holds.

Lemma 1: The integration operator (12) implies that $(\overline{\mathbf{p}}^s_j)_1 = 1$.

Proof: The result follows from the observation that the overlap regions are a disjoint set of regions which completely cover the source element,

$$J^s_j = \sum_{i=1}^{f^t} \sum_{n=1}^{N^{ov}_{i,j}} \left| \Omega^{ov(n)}_{i,j} \right|, \tag{15}$$

the requirement that $(\boldsymbol{\alpha}_j)_1(\mathbf{x}) = 1$ and the requirement that the quadrature rule must satisfy

$$\sum_{q=1}^{N_q} \hat{w}_q = 1. \quad \blacksquare \tag{16}$$

d. Building the set of adjacent faces

Define $\mathscr{F}^{s,adj} \subseteq \mathscr{F}^s$ as the set of $n_{j,adj}$ faces which are "adjacent" to $\mathscr{F}^s_j$ in some sense. Given a minimum size for $\mathscr{F}^{s,adj}$, this set is built as follows:

```
BuildAdjacentFaceSet(Face f, Integer min_size)
  AdjSet <- f
```

```
  while |AdjSet| < min_size
    add all edge neighbors of AdjSet faces to AdjSet
```

In most cases (and for the experiments performed in this paper), `min_size` is chosen to be equal to the number of coefficients in the polynomial expansion. However, for certain source grids this can lead to a poorly conditioned inversion problem when constructing the fit operator. In this case, it may be desired to increase the value of `min_size` as needed.

e. Building the local Fit Operator

There are two key properties that the fit operator must satisfy so that conservation and consistency are ensured. First, for conservation the fit operator must satisfy

$$(\overline{\mathbf{p}}_j^s)^T (\mathbf{F}_j^s)^{\oplus} = \mathbf{e}_1^T, \tag{17}$$

i.e. the average of the reconstruction over the source element must always yield its own density. For consistency, the fit operator must also satisfy

$$(\mathbf{F}_j^s)^{\oplus} \mathbf{1} = \mathbf{e}_1, \tag{18}$$

i.e. the fit operator must produce a constant reconstruction when fed the constant field. This claim is proven in the following theorem.

Theorem 1: If $(\mathbf{F}_j^s)^{\oplus}$ satisfies (17) and (18), the linear sub-map $\hat{\mathbf{R}}^{(j)} = (\mathsf{diag}\ \mathbf{J}_j^{ov})^{-1} \mathbf{P}_j (\mathbf{F}_j^s)^{\oplus}$ is conservative in $A = \{j\}$ and consistent in $B = \{i : \mathscr{F}_i^t \cap \mathscr{F}_j^s \neq \varnothing\}$.

Proof: Note that conservative and consistent linear sub-maps are defined in Ullrich and Taylor (2015) Definition 5 and 6. To show conservation: For all $k \in \{1, \ldots, f^s\}$, we have

$$\begin{aligned}
\sum_{i=1}^{f^t} (\hat{R}^{(j)})_{ik} \left(\sum_{\ell \in A} J^{ov}_{i,\ell} \right) &= \sum_{i=1}^{f^t} (\hat{R}^{(j)})_{ik} J^{ov}_{i,j}, \\
&= \sum_{m=1}^{N_c} (F^s_j)^{\oplus}_{mk} \sum_{i=1}^{f^t} (J^{ov}_{i,j})^{-1} (p^{ov}_{i,j})_m J^{ov}_{i,j}, \\
&= \sum_{m=1}^{N_c} (F^s_j)^{\oplus}_{mk} (\overline{p}^s_j)_m J^s_j && \text{by definition (14),} \\
&= J^s_j \delta_{j,k} && \text{by constraint (17),}
\end{aligned}$$

where $\delta_{j,k}$ is the Krönecker delta.

To show consistency:

$$\hat{\mathbf{R}}^{(j)} \mathbf{1} \quad = \quad (\mathbf{J}^{ov}_j)^{-1} \mathbf{P}_j (\mathbf{F}^s_j)^{\oplus} \mathbf{1} \quad \overset{(18)}{=} \quad (\mathbf{J}^{ov}_j)^{-1} \mathbf{P}_j \mathbf{e}_1,$$

then using (12) and $\boldsymbol{\alpha}(\mathbf{x}_{n,q})^T \mathbf{e}_1 = 1$,

$$(\hat{\mathbf{R}}^{(j)} \mathbf{1})_i \quad = \quad \begin{cases} (J^{ov}_{i,j})^{-1} \displaystyle\sum_{n=1}^{N^{ov}_{i,j}} |\Omega^{ov\,(n)}_{i,j}| \sum_{q=1}^{N_q} \hat{w}_q \quad = \quad 1, & \text{if } i \in B, \\ 0 & \text{otherwise.} \ \blacksquare \end{cases}$$

We now describe a technique for constructing the fit operator in terms of a weighted pseudoinverse. Define the density vector $\psi^{s,adj}_j$ as the vector of densities associated with the set $\mathscr{F}^{s,adj}$. A polynomial reconstruction is defined in $\mathscr{F}^s_j$ with coefficients $\mathbf{c}^s_j \in \mathbb{R}^{N_c}$. The operator $\mathbf{F}^s_j$ then denotes some approximate integration operator that maps the coefficients of the polynomial expansion to the discrete density over $\mathscr{F}^{s,adj}$,

$$\mathbf{F}^s_j \mathbf{c}^s_j \approx \psi^{s,adj}_j. \tag{19}$$

Note that equality will only hold if $N_c = n_{j,adj}$, which is generally not the case. For consistency with the integration operator in the source element, we require that $\mathbf{F}^s_j$ satisfy

$$(\mathbf{F}^s_j)_{1,:} = (\overline{\mathbf{p}}^s_j)^T. \tag{20}$$

The remaining components of $\mathbf{F}_j^s$, which represent the face-averaged integrals of the reconstruction over all adjacent elements, can be determined via any sufficiently high-order quadrature rule. For simplicity, we break up each adjacent element into triangular elements and use an integration procedure analogous to (12).

An equivalent weighted system to (19) can be computed by left-multipying both sides of this equality by a weighting matrix $\mathbf{W} \in \mathbb{R}^{n_{j,adj} \times n_{j,adj}}$,

$$\mathbf{W}\mathbf{F}_j^s \mathbf{c}_j^s \approx \mathbf{W}\psi_j^{s,adj}. \tag{21}$$

The purpose of the weighting matrix is to reduce the penalty associated with a mismatch between the polynomial reconstruction and the density $\psi_j^{s,adj}$ for faces farther away from $\mathscr{F}_j^s$. Many choices of $\mathbf{W}$ are available, although we have had empirical success with the choice

$$\mathbf{W} = \mathsf{diag}(\mathbf{w}^s)^{(N_p^s+2)}, \tag{22}$$

where $\mathbf{w}^s$ is the vector of graph distance away from the source element (so the source element has value zero, its edge neighbors have value 1, and so on).

High-order accuracy of the fit operator is now proven when the grid is refined uniformly, *i.e.* when refinements to the grid do not change the connectivity of finite volume faces. In this case we denote the average distance between grid points as Δx, and consider the limit of $\Delta x \to 0$.

Theorem 2: The weighted Moore-Penrose pseudoinverse $(\mathbf{W}\mathbf{F}_j^s)^+\mathbf{W}$ applied to densities $\psi_k^{s,adj}$ yields an order N_p^s reconstruction about $(\mathbf{x}_j^s)_0$ for a uniformly refined grid.

Proof: By properties of the pseudoinverse,

$$(\mathbf{W}\mathbf{F}_j^s)^+\mathbf{W}\mathbf{F}_j^s = \mathbf{I} \tag{23}$$

Consequently, for any polynomial up to degree $N_p^s - 1$, the operator $(\mathbf{W}\mathbf{F}_j^s)^+\mathbf{W}$ will yield the exact polynomial coefficients. To complete the proof, we must now demonstrate that for any field

$\psi(\mathbf{x}) = \alpha^u \beta^v$ with $u+v \geq N_p^s$ the reconstruction is $O(\Delta x^{N_p^s})$. Let q_k denote the total polynomial order of $(\boldsymbol{\alpha}_j)_k$, *i.e.*

$$(\boldsymbol{\alpha}_j(\mathbf{x}))_k = \alpha(\mathbf{x})^p \beta(\mathbf{x})^q \quad \Rightarrow \quad q_k = p+q. \tag{24}$$

Since entries of $\mathbf{F}_j^s$ are integrals of $\boldsymbol{\alpha}_j$, the k^{th} column of this operator must be $O(\Delta x^{q_k})$. For (23) to be satisfied it follows that the k^{th} row of $(\mathbf{W}\mathbf{F}_j^s)^+\mathbf{W}$ must then be $O(\Delta x^{-q_k})$. By construction, the densities of this field $\psi^{s,adj} = O(\Delta x^{u+v})$ and so $(\mathbf{c}_j^s)_k = (\mathbf{W}\mathbf{F}_j^s)^+\mathbf{W}\psi_j^{s,adj} = O(\Delta x^{u+v-q_k})$. Hence, the composed reconstruction must satisfy $\boldsymbol{\alpha}_j(\mathbf{x})^T\mathbf{c}_j^s = O(\Delta x^{u+v}) = O(\Delta x^{N_p^s})$. ■

As a consequence of Theorem 2, it is clear that $(\mathbf{W}\mathbf{F}_j^s)^+\mathbf{W}$ is a high-order accurate approximation to the fit operator. However, it can be readily demonstrated that this quantity does not lead to a conservative linear map, *i.e.*

$$(\overline{\mathbf{p}}_j^s)^T(\mathbf{W}\mathbf{F}_j^s)^+\mathbf{W} \neq \mathbf{e}_1^T. \tag{25}$$

Consequently, we define the corrected fit operator as follows:

$$(\mathbf{F}_j^s)^{\oplus} = \begin{cases} \mathbf{e}_1^T - (\overline{\mathbf{p}}_j^s)_{2:N_c}^T((\mathbf{W}\mathbf{F}_j^s)^+\mathbf{W})_{2:N_c,:}, & \text{in the first row,} \\ ((\mathbf{W}\mathbf{F}_j^s)^+\mathbf{W})_{2:N_c,:} & \text{in all other rows.} \end{cases} \tag{26}$$

It can then be shown that this operator satisfies all desired properties:

Theorem 3: The corrected fit operator (26) produces a conservative, consistent and order N_p^s accurate linear map.

Proof: By the definition of the fit operator and Lemma 1, it follows that $(\mathbf{F}_j^s)^{\oplus}$ satisfies (17). We now show consistency of $(\mathbf{F}_j^s)^{\oplus}$: For rows $m > 1$, since $(\mathbf{F}_j^s)_{:,1} = \mathbf{1}$ and satisfies (23), we have

$$(\mathbf{F}_j^s)_{2:N_c,m}^{\oplus}\mathbf{1} = \mathbf{0}. \tag{27}$$

For the first row, we have

$$
\begin{aligned}
(\mathbf{F}_j^s)^{\oplus}_{1,:}\mathbf{1} &= 1 - \sum_{m=1}^{N_{adj}} (\overline{\mathbf{p}}_j^s)^T_{2:N_c}((\mathbf{W}\mathbf{F}_j^s)^+\mathbf{W})_{2:N_c,m} \\
&= 1 - (\overline{\mathbf{p}}_j^s)^T_{2:N_c} \sum_{m=1}^{N_{adj}} ((\mathbf{W}\mathbf{F}_j^s)^+\mathbf{W})_{2:N_c,m} \\
&= 1 - (\overline{\mathbf{p}}_j^s)^T_{2:N_c} (\mathbf{F}_j^s)^{\oplus}_{2:N_c,:}\mathbf{1} \\
&= 1.
\end{aligned}
$$

Combining these results, it follows that $(\mathbf{F}_j^s)^{\oplus}$ satisfies (18). Hence, by Theorem 1 the composed linear map is conservative and consistent.

To show that the corrected operator retains order N_p^s accuracy, we first observe that the reconstruction coefficients associated with the non-constant mode are all identical to the uncorrected pseudoinverse, and hence retain the accuracy of that operation. For the constant mode, we are interested in computing the difference between the corrected and uncorrected fit operators,

$$
\mathbf{e}_1^T - (\overline{\mathbf{p}}_j^s)^T_{2:N_c}((\mathbf{W}\mathbf{F}_j^s)^+\mathbf{W})_{2:N_c,:} - ((\mathbf{W}\mathbf{F}_j^s)^+\mathbf{W})_{1,:}. \tag{28}
$$

Right-multiplying this difference by $\mathbf{F}_j^s$ and using (20) and Lemma 1 then leads to

$$
(\overline{\mathbf{p}}_j^s) - (\overline{\mathbf{p}}_j^s)^T_{2:N_c}((\mathbf{W}\mathbf{F}_j^s)^+\mathbf{W})_{2:N_c,:}\mathbf{F}_j^s - ((\mathbf{W}\mathbf{F}_j^s)^+\mathbf{W})_{1,:}\mathbf{F}_j^s = \mathbf{0}. \tag{29}
$$

This result implies that the correction to the first row does not lie in the polynomial space associated with $\mathbf{F}_j^s$, and so must be $O(\Delta x^{N_p^s})$. ■

f. Monotonicity

Monotonicity for the FV to FV remapping operator is guaranteed if and only if $N_c = 1$. In this case, the global linear remapping operator can be written directly as

$$
R_{ij} = \frac{|\Omega_{i,j}^{ov}|}{|\Omega_i^t|}. \tag{30}
$$

This operator simply assumes that the density variable is constant within each source mesh region, and that the amount of mass distributed to each target region is proportional to the overlap area. Conservation, consistency and monotonicity are trivially demonstrated in this case (Grandy 1999).

g. Results

Standard error norms for finite volume remapping from cubed-sphere meshes of resolution $n_e = 15, 30, 60$ (1350, 5400 and 21600 volumes) to a 1 degree great-circle regular latitude-longitude mesh (64800 volumes) with rectangular truncation and four orders of accuracy $N_p = 1, 2, 3, 4$ are given in Figure 2. Order $N_p + 1$ convergence in the L_1 error is mostly observed for all three fields, except for the smooth field at highest resolution and order of accuracy. In this case it appears that the falloff is due to ill-conditioning, likely from the underlying geometry (this effect appears to be consistent across all of the mapping schemes tested). Errors appear to be evenly distributed for the smooth field (not shown) and do not accumulate at the poles as one might expect. Nonetheless, for the relatively rough fields Y_{32}^{16} and Vortex, convergence rates are as expected. Absolute L_{min} and L_{max} error norms are reported for this test in Figure 3. Increased resolution appears to generally improve these errors, but clearly not as consistently as with the standard error norms. Consistently monotone behavior is only observed with np1, as expected. Also, these errors appear to improve greatly when going from a linear (np2) to a quadratic (np3) reconstruction, particularly for Y_2^2 and Vortex tests.

4. Finite Volume to GLL Finite Element Remapping

As opposed to the case of a finite volume target mesh, the integration operator for a finite element target mesh must couple together each of the degrees of freedom present in a target mesh element. Although mass can be distributed from a finite volume source region to a finite element target region relatively easily, one must be careful that mass is distributed to the degrees of freedom within each GLL element in a manner that is both consistent and conservative. For simplicity we consider the case of discontinuous GLL finite elements of order N_p^t and note that the procedure for constructing a map for continuous finite elements is analogous, except with a final application of a direct stiffness summation or averaging procedure.

As noted in Ullrich and Taylor (2015), calculation of $J_{i,j}^{ov}$ is difficult and relies on the fact that

$$J_i^t = \int_\Omega C_i(\mathbf{x}) dA, \tag{31}$$

where $C_i(\mathbf{x})$ is typically a non-linear test function associated with degree of freedom i, and the numerical integral is subject to effectively arbitrary underlying geometry. Hence, (31) may not hold in practice (particularly if J_i^t is evaluated using the pointwise determinant of the metric, rather than via an integration procedure). However, as long as the GLL finite element is geometrically consistent, it is nonetheless possible to construct a conservative, consistent and monotone linear map. The procedure described here builds the map without the need for constructing $J_{i,j}^{ov}$ explicitly.

a. Building the integration operator

The "first guess" integration operator is defined analogous to (12), except augmented with $C_i(\mathbf{x})$,

$$\mathbf{p}_{i,j}^{ov} = \sum_{n=1}^{N_{i,j}^{ov}} |\Omega_{i,j}^{ov\,(n)}| \sum_{q=1}^{N_q} \hat{w}_q C_i(\mathbf{x}_{n,q}) \boldsymbol{\alpha}_j(\mathbf{x}_{n,q})^T. \tag{32}$$

The source grid average is defined analogous to (14), except using (32) for $\mathbf{p}_{i,j}^{ov}$. Since the $C_i(\mathbf{x})$ represent a partition of unity it is also easy to show that Lemma 1 holds for this integrator.

Define $\overline{\mathbf{P}}_j \in \mathbb{R}^{f^t \times N_c}$ as the matrix where row i consists of $(J_i^t)^{-1} \mathbf{p}_{i,k}^{ov}$ (this represents the distribution of mass from $\mathscr{F}_j^s$ to all target elements). The composed global map then takes the form

$$\sum_{j=1}^{f^s} \overline{\mathbf{P}}_j (\mathbf{F}_j^s)^{\oplus}. \tag{33}$$

Although it can be readily shown that (33) is conservative, it is not consistent since the target grid weight is not determined by the inexact integration procedure inherited from the integration operator, *i.e.*

$$J_i^t \neq \sum_{j=1}^{f^s} \sum_{n=1}^{N_{i,j}^{ov}} |\Omega_{i,j}^{ov(n)}| \sum_{q=1}^{N_q} \hat{w}_q C_i(\mathbf{x}_{n,q}).$$

Here the mismatch is typically given by the minimum of the GLL quadrature order and the triangular quadrature order. To build a consistent map, we must modify the averaging operator to redistribute the integrated mass within the target element.

For each disjoint finite element $B \subseteq \{1,\ldots,f^t\}$ (with $i,k \in B \Rightarrow \Omega_i^t = \Omega_k^t$) define overlap regions between the finite volume mesh and finite element B as $\Omega_{B,j}^{ov} = \cup_{i\in B}\Omega_{i,j}^{ov}$ and the set of source volumes that overlap B as $\mathscr{V}_B = \{j \in [1,\ldots,f^s] : i \in B \Rightarrow \Omega_{i,j}^{ov} \neq \varnothing\}$. Then define a modified set of integration and averaging operators, denoted by $\tilde{\mathbf{P}}_j$, via

$$(\tilde{P}_j)_{km} = (\overline{P}_j)_{km}, \qquad \text{for } 1 < m \leq N_c, \tag{34}$$

and $(\tilde{P}_j)_{k1}$ as the solution of the least squares problem

$$\text{minimize} \quad \sum_{j=1}^{f^s} \sum_{k\in B} \left[(\tilde{P}_j)_{k1} - (\overline{P}_j)_{k1}\right]^2 \tag{35}$$

$$\text{subject to} \quad \sum_{j\in\mathscr{V}_B} (\tilde{P}_j)_{k1} = 1, \qquad \sum_{k\in B} J_k^t (\tilde{P}_j)_{k1} = |\Omega_{B,j}^{ov}|, \qquad (\overline{P}_j)_{k1} = 0 \Rightarrow (\tilde{P}_j)_{k1} = 0. \tag{36}$$

This procedure defines f^t minimization problems in $(|B| \times |\mathscr{V}_B|)$ free variables with $(|B| + |\mathscr{V}_B| - 1)$ constraints (one constraint is unnecessary due to a linear dependency). Note that for 2D GLL finite elements of order N_p^t we have $|B| = (N_p^t)^2$. This minimization problem can be trivially transformed into the minimization problem solved in Ullrich and Taylor (2015).

With the modified integration matrix, the composed linear map takes the form

$$\mathbf{R} = \sum_{j=1}^{f^s} \tilde{\mathbf{P}}_j (\mathbf{F}_j^s)^{\oplus}. \tag{37}$$

Note that the modified integration operators retain the same source grid average as $\overline{\mathbf{P}}_j$:

Lemma 2: The modified operators $\tilde{\mathbf{P}}_j$ satisfy

$$(\mathbf{J}^t)^T(\tilde{\mathbf{P}}_j) = J_j^s(\overline{\mathbf{p}}_j^s)^T. \tag{38}$$

Proof: For columns $m > 1$ the result follows immediately from (34) and the definition of $\overline{\mathbf{P}}_j$. For column $m = 1$ we have from (36),

$$(\mathbf{J}^t)^T(\tilde{\mathbf{P}}_j)_{:,1} = \sum_{k=1}^{f^t} J_k^t(\tilde{P}_j)_{k1} = \sum_B |\Omega_{B,j}^{ov}| = J_j^s, \tag{39}$$

which satisfies the lemma since $(\overline{\mathbf{p}}_j^s)_1 = 1$. ■

The key result of this section then follows:

Theorem 5: The linear map $\mathbf{R}$, as defined by (37), is conservative and consistent.

Proof: Conservation and consistency for linear maps are determined by Ullrich and Taylor (2015) Proposition 1 and 2. Conservation follows from Lemma 2,

$$(\mathbf{J}^t)^T\mathbf{R} \overset{(37)}{=} (\mathbf{J}^t)^T \sum_{j=1}^{f^s} \tilde{\mathbf{P}}_j(\mathbf{F}_j^s)^{\oplus} \overset{\text{(Lemma 2)}}{=} \sum_{j=1}^{f^s} J_j^s(\overline{\mathbf{p}}_j^s)^T(\mathbf{F}_j^s)^{\oplus} \overset{(17)}{=} \sum_{j=1}^{f^s} J_j^s\mathbf{e}_j^T = (\mathbf{J}^s)^T.$$

And consistency from the definition of $\tilde{\mathbf{P}}_j$,

$$\mathbf{R1} \overset{(37)}{=} \sum_{j=1}^{f^s} \tilde{\mathbf{P}}_j(\mathbf{F}_j^s)^{\oplus}\mathbf{1} \overset{(18)}{=} \sum_{j=1}^{f^s} \tilde{\mathbf{P}}_j\mathbf{e}_1 \overset{(36)}{=} 1. \quad \blacksquare \tag{40}$$

b. Monotonicity

The linear map (37) can be rendered monotone by choosing a piecewise constant reconstruction on the FV mesh ($N_c = 1$) and by leveraging the strategy of Ullrich and Taylor (2015) to remove negative coefficients from $\tilde{\mathbf{P}}_j$. In practice, this option tends to underperform the volumetric strategy discussed in the following section, and so is not analyzed in this paper.

c. Results

Standard error norms are reported in Figure 4 for finite volume to finite element remapping from cubed-sphere meshes of resolution $n_e = 15, 30, 60$ (1350, 5400 and 21600 volumes) to a tessellated $n_e = 30$ cubed-sphere mesh (10800 elements) with rectangular truncation and three orders of accuracy $N_p^s = 2, 3, 4$ and $N_p^t = 4$ on the target mesh. Convergence order is between N_p^s and $N_p^s + 1$ in each norm, where error norms are again observed to level off at the highest order and for the smoothest field. Again, for the relatively rough fields Y_{32}^{16} and Vortex, convergence rates are as expected, even tending towards order $N_p^s + 1$ convergence. Absolute L_{min} and L_{max} error norms are reported for this test in Figure 5. The behavior of these norms is analogous to that of the finite volume maps. Monotonicity is not generally expected in this case, even for np1, since the piecewise constant field is being mapped onto a fourth-order basis function which falls out of the range $[0, 1]$. These errors again appear to improve greatly when going from a linear (np2) to a quadratic (np3) reconstruction, particularly for Y_2^2 and Vortex tests.

5. Finite Volume to GLL Finite Element Remapping (Volumetric)

In this section an alternative approach is pursued for monotone remapping from finite volumes to GLL finite elements, similar to an algorithm implemented in the Earth System Modeling Framework (Hill et al. 2004). Under this approach an artificial set of control volumes (CVs) are introduced for each of the degrees of freedom on the finite element mesh. By treating the CVs as finite volumes, the FV to FV remapping techniques described in section 3 can be directly employed.

The CVs in the reference element are chosen so that the geometric area of each CV equates to the quadrature weight of that node. For example, for fourth-order GLL quadrature with weights $\left[\frac{1}{6}, \frac{5}{6}, \frac{5}{6}, \frac{1}{6}\right]$ over the reference element $[-1, 1]$, CV edges are placed at $\alpha = \left[-1, -\frac{5}{6}, 0, \frac{5}{6}, 1\right]$. However, deformation of the mesh due to the unstructured grid and spherical geometry means this correspondence is not maintained away from the reference element. In particular, the CV areas, denoted by $|\hat{\Omega}_i^t|$ will not generally agree with the local weights J_i^t, and so cannot be used directly to obtain a conservative and consistent map. A depiction of the artificial CVs is given in Figure 6 for fourth-order GLL finite elements.

a. Building the linear map

The linear map is defined as

$$\mathbf{R} = (\mathsf{diag}\,\mathbf{J}^t)^{-1}\mathbf{A}\sum_{j=1}^{f^s}\mathbf{P}_j(\mathbf{F}_j^s)^{\oplus}, \tag{41}$$

where $\mathbf{P}_j$ and $(\mathbf{F}_j^s)^{\oplus}$ are the integration / averaging (section 3.c) and fit operators (section 3.e) from the FV to FV map formulation. The operator $\mathbf{A} \in \mathbb{R}^{f^t \times f^t}$ is a redistribution operator that accounts for the fact that $|\hat{\Omega}_i^t|$ and J_i^t are generally not equal. It is computed as follows:

For each disjoint finite element $B \subseteq \{1, \ldots, f^t\}$, define the local redistribution operator $\mathbf{A}_B \in \mathbb{R}^{f^t \times f^t}$ as $(\mathbf{A}_B)_{ik} = 0$ if $i \notin B$ or $k \notin B$ and otherwise determined from the least squares problem

$$\text{minimize} \quad \sum_{i\in B}\sum_{k\in B}\left[(\mathbf{A}_B)_{ik} - \delta_{ik}\right]^2 \tag{42}$$

$$\text{subject to} \quad \sum_{i\in B}(\mathbf{A}_B)_{ik} = 1, \qquad \sum_{k\in B}|\hat{\Omega}_k^t|(\mathbf{A}_B)_{ik} = J_i^t, \tag{43}$$

where δ_{ik} is the Krönecker delta. Observe that if $J_i^t = |\hat{\Omega}_i^t|$ for each degree of freedom then the solution is trivially given by the identity operator over B. The total redistribution operator can then be written as

$$\mathbf{A} = \sum_B \mathbf{A}_B. \tag{44}$$

Each $\mathbf{A}_B$ is effectively a sub-map within the finite element from CVs to quadrature points. As a consequence, monotonicity of this map can be enforced following the procedure described in Ullrich and Taylor (2015) section 3.e. Note that if the finite volume to CV map is monotonic (guaranteed for $N_c = 1$) and the redistribution $\mathbf{A}$ is monotonic then the composed map will also be monotonic.

With the conditions (43), the composed linear map (41) is then readily shown to satisfy the conservative and consistency constraints:

Theorem 6: The linear map $\mathbf{R}$, as defined by (41), is conservative and consistent.

Proof: To show conservation,

$$(\mathbf{J}^t)^T \mathbf{R} = \mathbf{1}^T \mathbf{A} \sum_{j=1}^{f^s} \mathbf{P}_j (\mathbf{F}_j^s)^{\oplus} \overset{(43)}{=} \mathbf{1}^T \sum_{j=1}^{f^s} \mathbf{P}_j (\mathbf{F}_j^s)^{\oplus} \overset{(14)}{=} \sum_{j=1}^{f^s} J_j^s (\overline{\mathbf{p}}_j^s)^T (\mathbf{F}_j^s)^{\oplus} \overset{(17)}{=} \sum_{j=1}^{f^s} J_j^s \mathbf{e}_j^T = (\mathbf{J}^s)^T \tag{45}$$

And to show consistency,

$$\mathbf{R1} = (\mathsf{diag}\ \mathbf{J}^t)^{-1} \mathbf{A} \sum_{j=1}^{f^s} \mathbf{P}_j (\mathbf{F}_j^s)^{\oplus} \mathbf{1} \overset{(18)}{=} (\mathsf{diag}\ \mathbf{J}^t)^{-1} \mathbf{A} \sum_{j=1}^{f^s} \mathbf{P}_j \mathbf{e}_1 \overset{(12)}{=} (\mathsf{diag}\ \mathbf{J}^t)^{-1} \mathbf{A} |\hat{\Omega}^t| \overset{(43)}{=} \mathbf{1}. \quad \blacksquare \tag{46}$$

b. Results

Standard error norms are reported in Figure 7 for finite volume to finite element remapping from cubed-sphere meshes of resolution $n_e = 15, 30, 60$ (1350, 5400 and 21600 volumes) to a tessellated $n_e = 30$ cubed-sphere mesh (10800 elements) with a first-order (monotone) finite volume reconstruction ($N_c = 1$) and three orders of accuracy $N_p^t = 2, 3, 4$ on the target mesh. Convergence order is between 1 and 2 in each norm. Errors are dominated by the quality of the reconstruction on the source grid, and so do not improve with target grid order. Monotonicity is validated in Figure 8, which depicts L_{min} and L_{max} and shows no overshoots or undershoots.

6. Finite Element to Finite Element Remapping

The final procedure discussed in this paper addresses mapping from a finite element source mesh (with order of accuracy N_p^s) to a finite element target mesh (with order of accuracy N_p^t).

The conservative map between finite elements is constructed using Galerkin projection, analogous to the procedure described in Farrell (2009); Farrell et al. (2009); Farrell and Maddison (2011). Specifically, we assume that the continuous field can be expanded on the source mesh as

$$\psi(\mathbf{x}) = \sum_{j=1}^{f^s} \psi_j^s C_j^s(\mathbf{x}), \tag{47}$$

and on the target mesh as

$$\psi(\mathbf{x}) = \sum_{i=1}^{f^t} \psi_i^t C_i^t(\mathbf{x}), \tag{48}$$

where $C_j^s(\mathbf{x})$ and $C_i^t(\mathbf{x})$ denote the basis functions on the source and target mesh. Equating (47) and (48), multiplying through by $C_k^t(\mathbf{x})$ and integrating over the domain then leads to

$$\sum_{j=1}^{f^s} \psi_j^s \int_\Omega C_j^s(\mathbf{x}) C_k^t(\mathbf{x}) dV = \sum_{i=1}^{f^t} \psi_i^t \int_\Omega C_i^t(\mathbf{x}) C_k^t(\mathbf{x}) dV. \tag{49}$$

So as to avoid inverting a linear system mass lumping is applied (Farrell 2009),

$$\int_\Omega C_i^t(\mathbf{x}) C_k^t(\mathbf{x}) dV \approx \mathsf{diag}\left[\int_\Omega C_i^t(\mathbf{x}) \left(\sum_{m=1}^{f^t} C_m^t\right) dV\right] = \mathsf{diag}\left(\int_\Omega C_i^t(\mathbf{x}) dV\right). \tag{50}$$

Consequently, the Galerkin expansion implies a linear map of the form

$$\psi_i^t = \sum_{j=1}^{f^s} \left[\mathsf{diag}\left(\int_\Omega C_i^t(\mathbf{x}) dV\right)\right]^{-1} \left[\int_\Omega C_i^t(\mathbf{x}) C_j^s(\mathbf{x}) dV\right] \psi_j^s \quad \Longleftrightarrow \quad \psi^t = \hat{\mathbf{R}} \psi^s. \tag{51}$$

a. Building the discrete map

The map (51) is conservative and consistent for exact integration, but only approximately satisfies these conditions when inexact integration is used. This section is primarily concerned with the case when exact integration is unavailable. To proceed, the integrated overlap area between each source grid element and target basis function is first approximated using inexact triangular quadrature via

$$\hat{J}_{i,j}^{ov} = \sum_{n=1}^{N_{i,j}^{ov}} \left|\Omega_{i,j}^{ov(n)}\right| \sum_{q=1}^{N_q} \hat{w}_q C_i^t(\mathbf{x}_{n,q}), \tag{52}$$

which leads to approximate global integrals of the basis functions $\hat{J}_i^t$ via

$$\hat{J}_i^t = \sum_{j=1}^{f^s} \hat{J}_{ij}^{ov}. \tag{53}$$

A finite element to finite element map is constructed in two stages: First, for each source element B^s a conservative map $\hat{\mathbf{R}}_{B^s}$ is constructed that maps the element to degrees of freedom on the target mesh. Second, for each target element B^t an operator $\mathbf{A}_{B^t}$ is constructed that redistributes mass so that the composed map maintains consistency. The composed map is then expanded as

$$\mathbf{R} = \left(\mathsf{diag}\ \mathbf{J}^t\right)^{-1} \left(\sum_{B^t} \mathbf{A}_{B^t}\right) \left(\sum_{B^s} \left(\mathsf{diag}\ \hat{\mathbf{J}}_{B^s}^{ov}\right) \hat{\mathbf{R}}_{B^s}\right), \tag{54}$$

where $\hat{\mathbf{J}}_{B^s}^{ov} \in \mathbb{R}^{f^t}$ denotes the vector of approximate overlap areas associated with B^s and obtained from (52).

The coefficients of a "first-guess" Gaussian projection map are computed approximately, again using triangular quadrature,

$$\left(\tilde{\mathbf{R}}_{B^s}\right)_{ij} = \frac{1}{\hat{J}_{ij}^{ov}} \sum_{n=1}^{N_{i,j}^{ov}} \left|\Omega_{i,j}^{ov\,(n)}\right| \sum_{q=1}^{N_q} \hat{w}_q C_i^t(\mathbf{x}_{n,q}) C_j^s(\mathbf{x}_{n,q}) \qquad (j \in B^s). \tag{55}$$

The conservative map is then obtained via the least squares problem

$$\text{minimize} \quad \sum_{j\in B^s} \sum_{i=1}^{f^t} \left[(\hat{\mathbf{R}}_{B^s})_{ij} - (\tilde{\mathbf{R}}_{B^s})_{ij}\right]^2 \tag{56}$$

$$\text{subject to} \quad \sum_{j\in B^s} (\hat{\mathbf{R}}_{B^s})_{ij} = 1, \qquad \sum_{i=1}^{f^t} \hat{J}_{ij}^{ov} (\hat{\mathbf{R}}_{B^s})_{ij} = J_j^s. \tag{57}$$

The redistribution operator $\mathbf{A}_{B^t}$ is constructed analogous to the procedure in section 5.a. For each finite element $B^t \subseteq \{1,\ldots,f^t\}$, define the local redistribution operator $\mathbf{A}_{B^t} \in \mathbb{R}^{f^t\times f^t}$ as $(\mathbf{A}_{B^t})_{ik} = 0$ if $i \notin B^t$ or $k \notin B^t$ and otherwise determined from the least squares problem

$$\text{minimize} \quad \sum_{i\in B^t} \sum_{k\in B^t} \left[(\mathbf{A}_{B^t})_{ik} - \delta_{ik}\right]^2 \tag{58}$$

$$\text{subject to} \quad \sum_{k\in B^t} (\mathbf{A}_{B^t})_{ik} = 1, \qquad \sum_{i\in B^t} \hat{J}_i^t (\mathbf{A}_{B^t})_{ik} = J_k^t. \tag{59}$$

Attaining the expected order of accuracy ($\min(N_p^s, N_p^t)$) of this approach is reliant on $\tilde{\mathbf{R}}_{B^s}$ and $\hat{J}_{ij}^{ov}$ as being convergent to the quantities associated with the exact Galerkin projection map, which is in turn satisfied up to the order of accuracy of the triangular quadrature rule. Accuracy also requires that J_j^s and J_i^t being chosen such that

$$J_j^s = \int_\Omega C_j^s(\mathbf{x})dV + O(\Delta x^{N_p^s}), \quad \text{and} \quad J_i^t = \int_\Omega C_i^s(\mathbf{x})dV + O(\Delta x^{N_p^t}). \tag{60}$$

We now prove the key result for this section:

Theorem 7: The linear map, defined by (54) is conservative and consistent.

Proof: Denote the global redistribution operator by

$$\mathbf{A} = \sum_{B^t} \mathbf{A}_{B^t}. \tag{61}$$

To show conservation,

$$(\mathbf{J}^t)^T \mathbf{R} = \mathbf{1}^T \mathbf{A} \left(\sum_{B^s} \left(\mathsf{diag}\ \hat{\mathbf{J}}_{B^s}^{ov}\right) \hat{\mathbf{R}}_{B^s} \right) \overset{(59)}{=} \mathbf{1}^T \sum_{B^s} \left(\mathsf{diag}\ \hat{\mathbf{J}}_{B^s}^{ov}\right) \hat{\mathbf{R}}_{B^s} = \sum_{B^s} \sum_{i=1}^{f^t} \hat{J}_{ij}^{ov} \hat{\mathbf{R}}_{B^s} \overset{(57)}{=} \mathbf{J}_j^s. \tag{62}$$

And to show consistency,

$$\begin{aligned} \mathbf{R1} &= \left(\mathsf{diag}\ \mathbf{J}^t\right)^{-1} \mathbf{A} \left(\sum_{B^s} \left(\mathsf{diag}\ \hat{\mathbf{J}}_{B^s}^{ov}\right) \hat{\mathbf{R}}_{B^s} \mathbf{1} \right) \\ &\overset{(53)}{=} \left(\mathsf{diag}\ \mathbf{J}^t\right)^{-1} \mathbf{A} \sum_{B^s} \left(\mathsf{diag}\ \hat{\mathbf{J}}_{B^s}^{ov}\right) = \left(\mathsf{diag}\ \mathbf{J}^t\right)^{-1} \mathbf{A} \hat{\mathbf{J}}^t \overset{(59)}{=} \mathbf{1}. \quad \blacksquare \end{aligned} \tag{63}$$

b. Results

Standard error norms are reported in Figure 9 for finite element remapping from cubed-sphere meshes of resolution $n_e = 15, 30, 60$ (1350, 5400 and 21600 volumes) to a tessellated $n_e = 30$ cubed-sphere mesh (10800 elements) with three orders of accuracy $N_p^s = N_p^t = 2, 3, 4$. Convergence order is between N_p^s and $N_p^s + 1$ in each norm. Again we observe a flattening of the error curve at the highest resolution and order of accuracy for the smooth field. Figure 10 depicts L_{min} and L_{max}. There is no evidence of overshoots or undershoots for np2, which corresponds to a bilinear reconstruction, but both overshoots and undershoots are observed at higher orders of accuracy.

7. Conclusions

This paper has introduced four new algorithms for the generation of arbitrary-order conservative and consistent (and optionally monotone) linear maps between fields on unstructured spherical meshes using the theory of Ullrich and Taylor (2015). These include maps (a) between two finite volume meshes, (b) from finite volume to finite element meshes using a projection-type approach, (c) from finite volume to finite element meshes using volumetric integration and (d) between two finite element meshes. A theoretical foundation has been provided in each case to demonstrate that these maps satisfy the desired properties. These maps are useful for coupling together model components that are defined using different grid systems or for post-procesing of model data. Future work will focus on non-linear coupling of linear maps to produce high-order accuracy in smooth solution regions and adoption of these techniques in the context of semi-Lagrangian advection.

a. Software availability

The software described in this manuscript has been released as part of the Tempest software package, and is available for use under the Lesser GNU Public License (LGPL). All software can be obtained from GitHub via the following clone URL:

`https://github.com/ClimateGlobalChange/tempestremap.git`

b. Acknowledgements

The authors would like to thank Mark Taylor for spurring this work and Miranda Mundt for her quality assurance efforts, particularly with the volumetric formulation. The authors would also like to thank Iulian Grindeanu for helpful discussions on the development of these algorithms. This project is funded through the Department of Energy, Office of Science, Division for Advanced Scientific Computing Research and the “Multiscale Methods for Accurate, Efficient, and Scale-Aware Models of the Earth System” program.

References

Chesshire, G., and W. Henshaw, 1994: A scheme for conservative interpolation on overlapping grids. *SIAM Journal on Scientific Computing*, **15 (4)**, 819–845, doi:10.1137/0915051.

Farrell, P., and J. Maddison, 2011: Conservative interpolation between volume meshes by local galerkin projection. *Computer Methods in Applied Mechanics and Engineering*, **200 (1)**, 89–100, doi:10.1016/j.cma.2010.07.015.

Farrell, P., M. Piggott, C. Pain, G. Gorman, and C. Wilson, 2009: Conservative interpolation between unstructured meshes via supermesh construction. *Computer Methods in Applied Mechanics and Engineering*, **198 (33)**, 2632–2642, doi:10.1016/j.cma.2009.03.004.

Farrell, P. E., 2009: Galerkin projection of discrete fields via supermesh construction. Ph.D. thesis, Imperial College London.

Garimella, R., M. Kucharik, and M. Shashkov, 2007: An efficient linearity and bound preserving conservative interpolation (remapping) on polyhedral meshes. *Computers & fluids*, **36 (2)**, 224–237, doi:10.1016/j.compfluid.2006.01.014.

Giraldo, F. X., 2001: A spectral element shallow water model on spherical geodesic grids. *International Journal for Numerical Methods in Fluids*, **35 (8)**, 869–901, doi:10.1002/1097-0363(20010430)35:8⟨869::AID-FLD116⟩3.0.CO;2-S.

Grandy, J., 1999: Conservative remapping and region overlays by intersecting arbitrary polyhedra. *Journal of Computational Physics*, **148 (2)**, 433–466, doi:10.1006/jcph.1998.6125.

Guba, O., M. A.Taylor, P. A. Ullrich, J. R. Overvelt, and M. N. Levy, 2014: The spectral element method on variable resolution grids: evaluating grid sensitivity and resolution-aware numerical viscosity. *Geoscientific Model Development*, **7**, 2803 – 2816, doi:10.5194/gmd-7-2803-2014.

Hill, C., C. DeLuca, M. Suarez, A. Da Silva, and Coauthors, 2004: The architecture of the Earth System Modeling Framework. *Computing in Science & Engineering*, **6 (1)**, 18–28, doi:10.1109/MCISE.2004.1255817.

Jalali, A., and C. Ollivier-Gooch, 2013: Higher-order finite volume solution reconstruction on highly anisotropic meshes. *AIAA paper*, **2565**, 2013.

Jiao, X., and M. T. Heath, 2004: Common-refinement-based data transfer between non-matching meshes in multiphysics simulations. *International Journal for Numerical Methods in Engineering*, **61 (14)**, 2402–2427, doi:10.1002/nme.1147.

Jones, P. W., 1999: First- and second-order conservative remapping schemes for grids in spherical coordinates. *Mon. Weather Rev.*, **127**, 2204–2210, doi:10.1175/1520-0493(1999)127⟨2204:FASOCR⟩2.0.CO;2.

Lauritzen, P. H., and R. D. Nair, 2007: Monotone and conservative cascade remapping between spherical grids (CaRS): Regular latitude-longitude and cubed-sphere grids. *Mon. Weather Rev.*, **136**, 1416–1432, doi:10.1175/2007MWR2181.1.

Menon, S., and D. P. Schmidt, 2011: Conservative interpolation on unstructured polyhedral meshes: An extension of the supermesh approach to cell-centered finite-volume variables. *Computer Methods in Applied Mechanics and Engineering*, **200 (41)**, 2797–2804, doi:10.1016/j.cma.2011.04.025.

Ullrich, P. A., P. H. Lauritzen, and C. Jablonowski, 2009: Geometrically exact conservative remapping (GECoRe): Regular latitude-longitude and cubed-sphere grids. *Mon. Weather Rev.*, **137 (6)**, 1721–1741, doi:10.1175/2008MWR2817.1.

Ullrich, P. A., and M. A. Taylor, 2015: Arbitrary-Order Conservative and Consistent Remapping and a Theory of Linear Maps, Part 1. *Mon. Weather Rev.*, **143**, 2419–2440, doi:10.1175/MWR-D-14-00343.1.

Weller, H., 2013: Non-orthogonal version of the arbitrary polygonal C-grid and a new diamond grid. *Geoscientific Model Development*, **7**, 779–797, doi:10.5194/gmd-7-779-2014.

LIST OF FIGURES

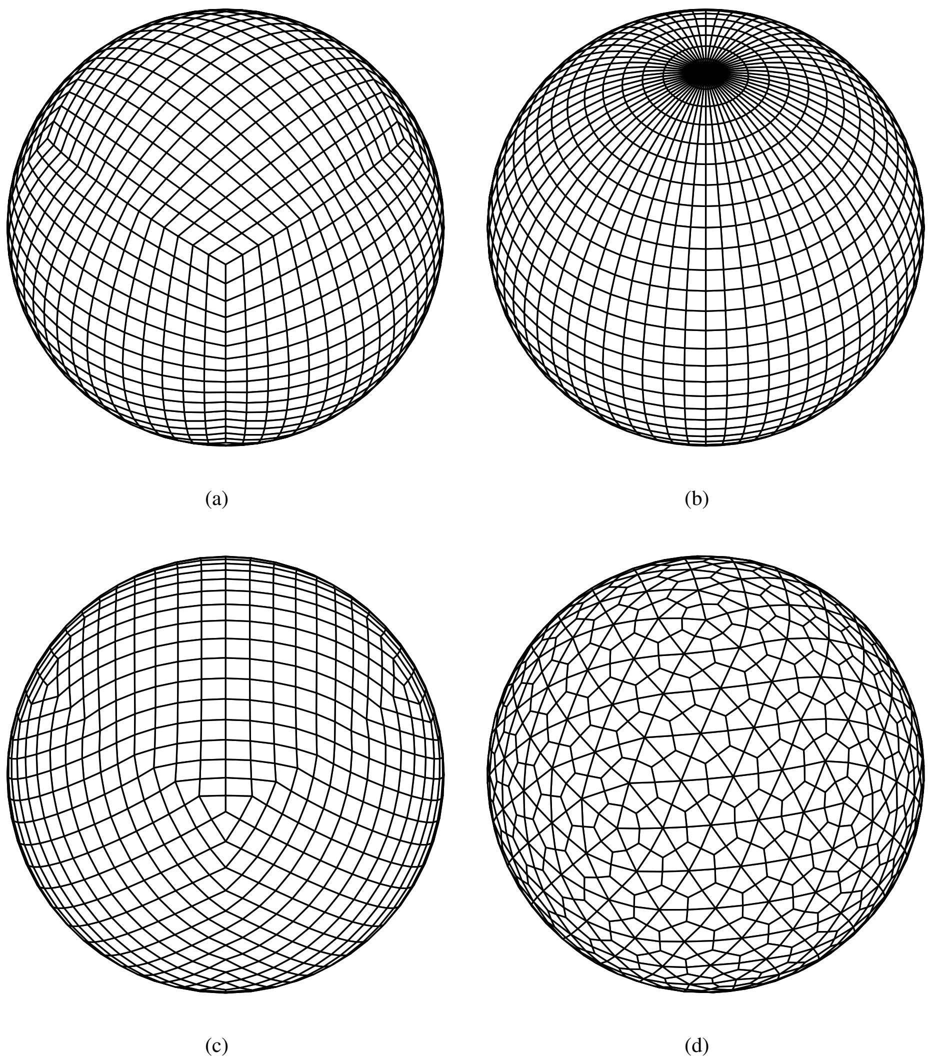

FIG. 1: A depiction of the four meshes studied in this manuscript: (a) Cubed-sphere, (b) Great-circle latitude-longitude, (c) tessellated cubed-sphere and (d) icosahedral flag grid.

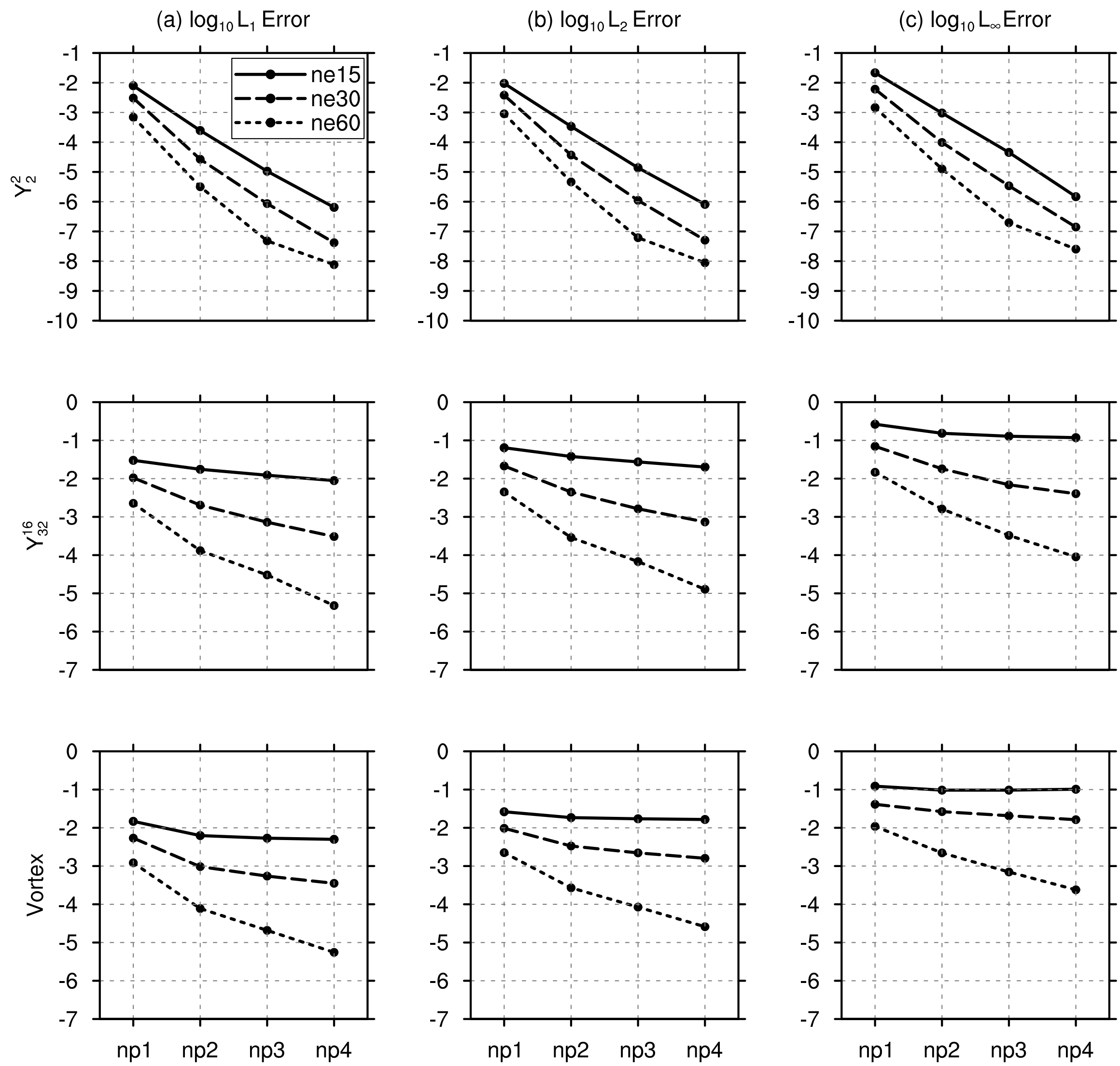

FIG. 2: Standard L_1, L_2 and L_∞ error norms reported for conservative and consistent remapping of the three idealized fields from the cubed-sphere mesh to the 1 degree great-circle regular latitude-longitude mesh for cubed-sphere resolutions $n_e = 15, 30, 60$, rectangular truncation and for four orders of accuracy $N_p = 1, 2, 3, 4$.

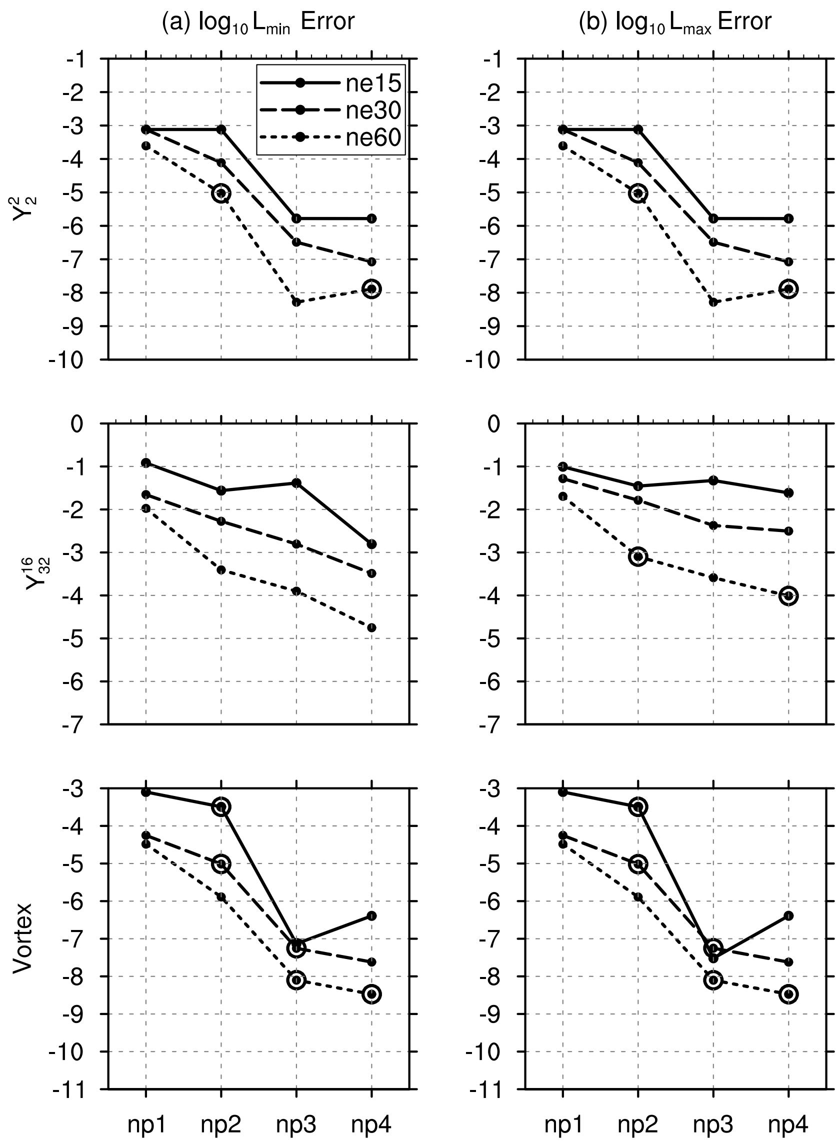

FIG. 3: Absolute L_{min} and L_{max} error norms reported for conservative and consistent remapping of the three idealized fields from the cubed-sphere mesh to the 1 degree great circle regular latitude-longitude mesh for cubed-sphere resolutions $n_e = 15, 30, 60$, rectangular truncation and for three orders of accuracy $N_p = 2, 3, 4$. Undershoots (left) and overshoots (right) are indicated by circled data points.

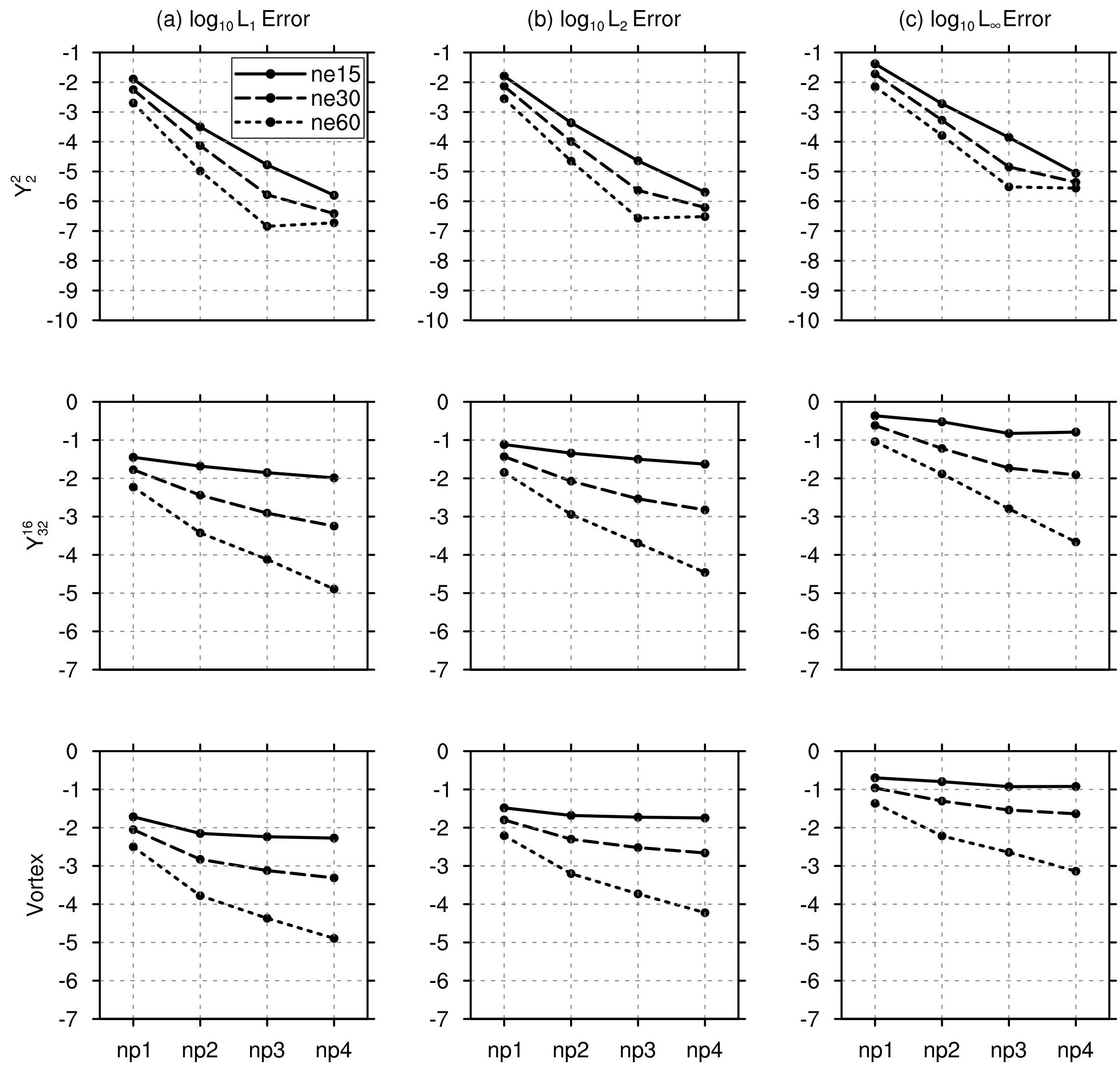

FIG. 4: Standard L_1, L_2 and L_∞ error norms reported for conservative, consistent and monotone remapping of the three idealized fields from the finite-volume cubed-sphere mesh to the tessellated $n_e = 30$ cubed-sphere mesh for source mesh cubed-sphere resolutions $n_e = 15, 30, 60$, rectangular truncation and for four orders of accuracy $N_p^s = 2, 3, 4$ on the source mesh and $N_p^t = 4$ on the target mesh.

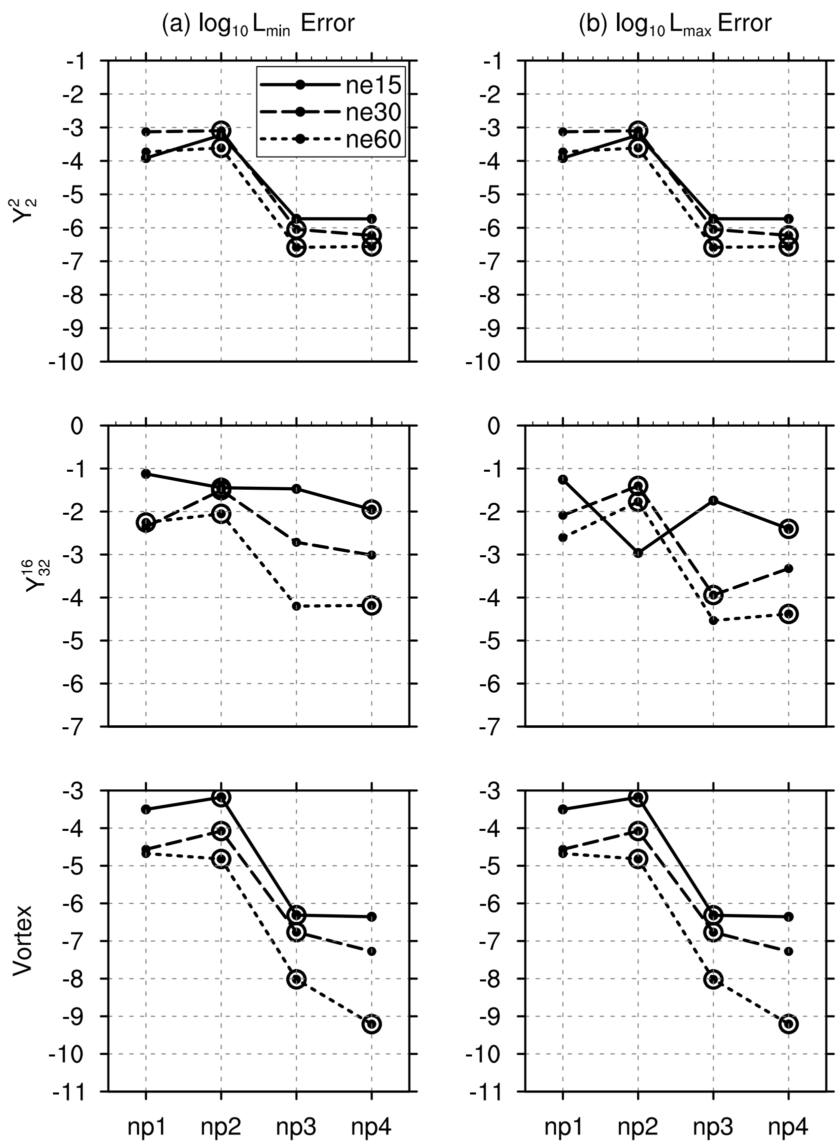

FIG. 5: Absolute L_{min} and L_{max} error norms reported for conservative and consistent remapping of the three idealized fields from the finite-volume cubed-sphere mesh to the tessellated $n_e = 30$ cubed-sphere mesh for source mesh cubed-sphere resolutions $n_e = 15, 30, 60$, rectangular truncation and for four orders of accuracy $N_p^s = 2, 3, 4$ on the source mesh and $N_p^t = 4$ on the target mesh. Undershoots (left) and overshoots (right) are indicated by circled data points.

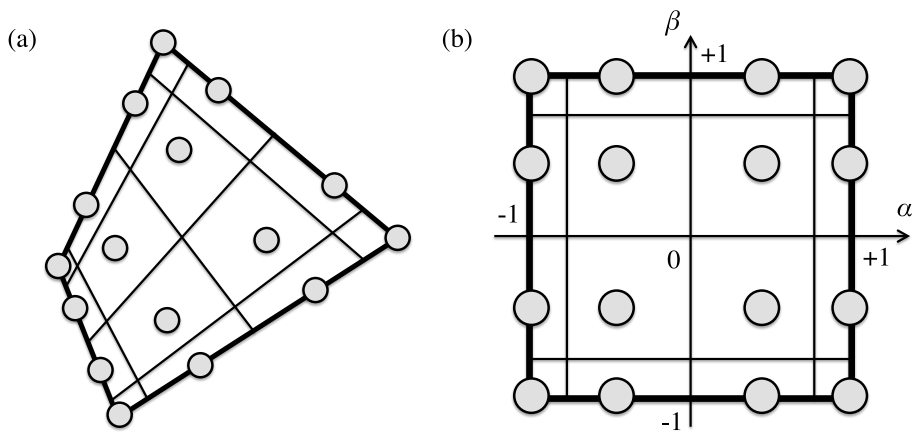

FIG. 6: (a) Artificial control volumes associated with degrees of freedom in a fourth-order Gauss-Lobatto-Legendre finite element and associated GLL quadrature nodes. (b) Artificial control volumes in the fourth-order Gauss-Lobatto-Legendre reference element and associated GLL quadrature nodes, with coordinate axes $\alpha \in [-1,1]$ and $\beta \in [-1,1]$.

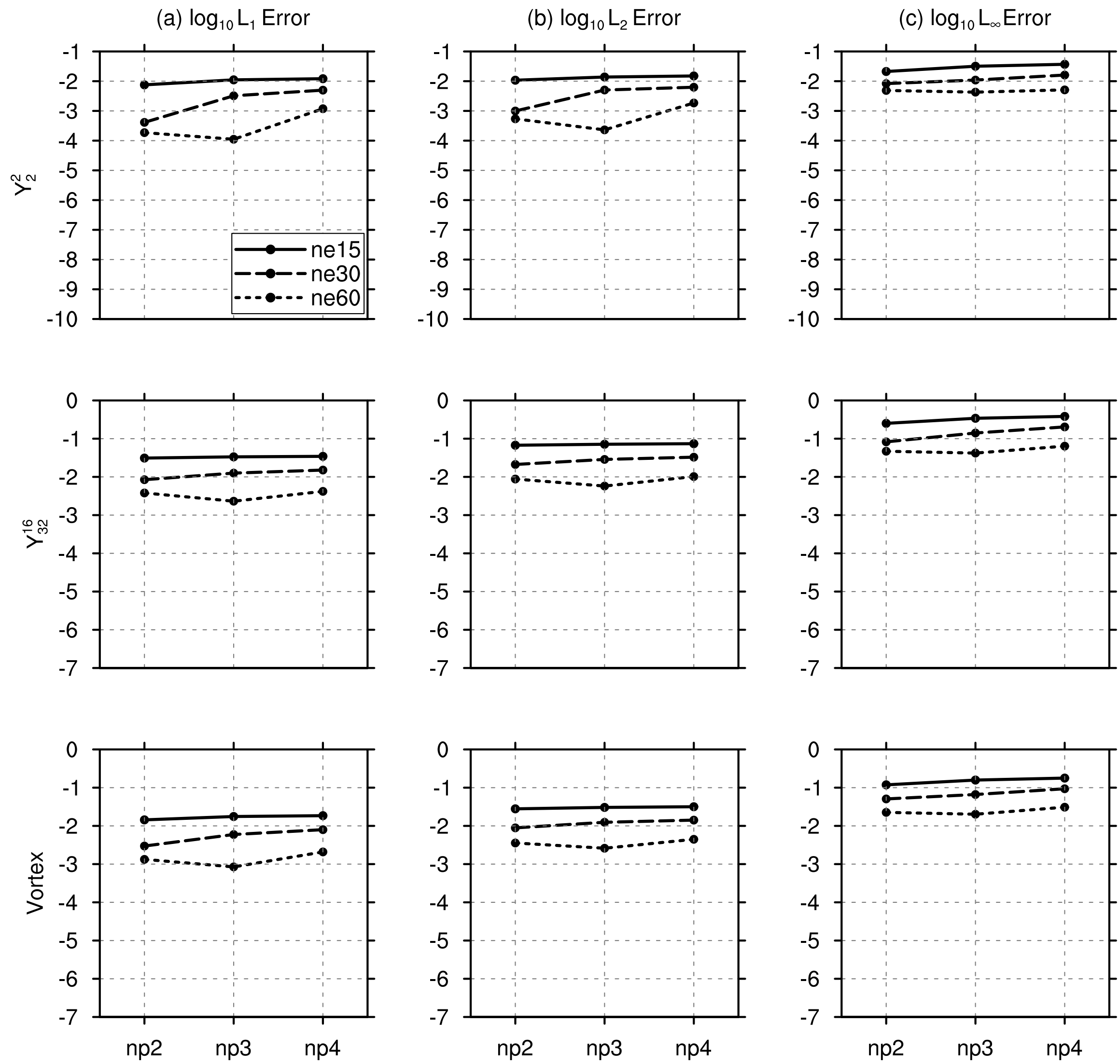

FIG. 7: Standard L_1, L_2 and L_∞ error norms reported for conservative, consistent and monotone remapping of the three idealized fields from the finite-volume cubed-sphere mesh to the tessellated $n_e = 30$ cubed-sphere mesh for source mesh cubed-sphere resolutions $n_e = 15, 30, 60$, rectangular truncation and for four orders of accuracy $N_p^t = 2, 3, 4$ on the target mesh.

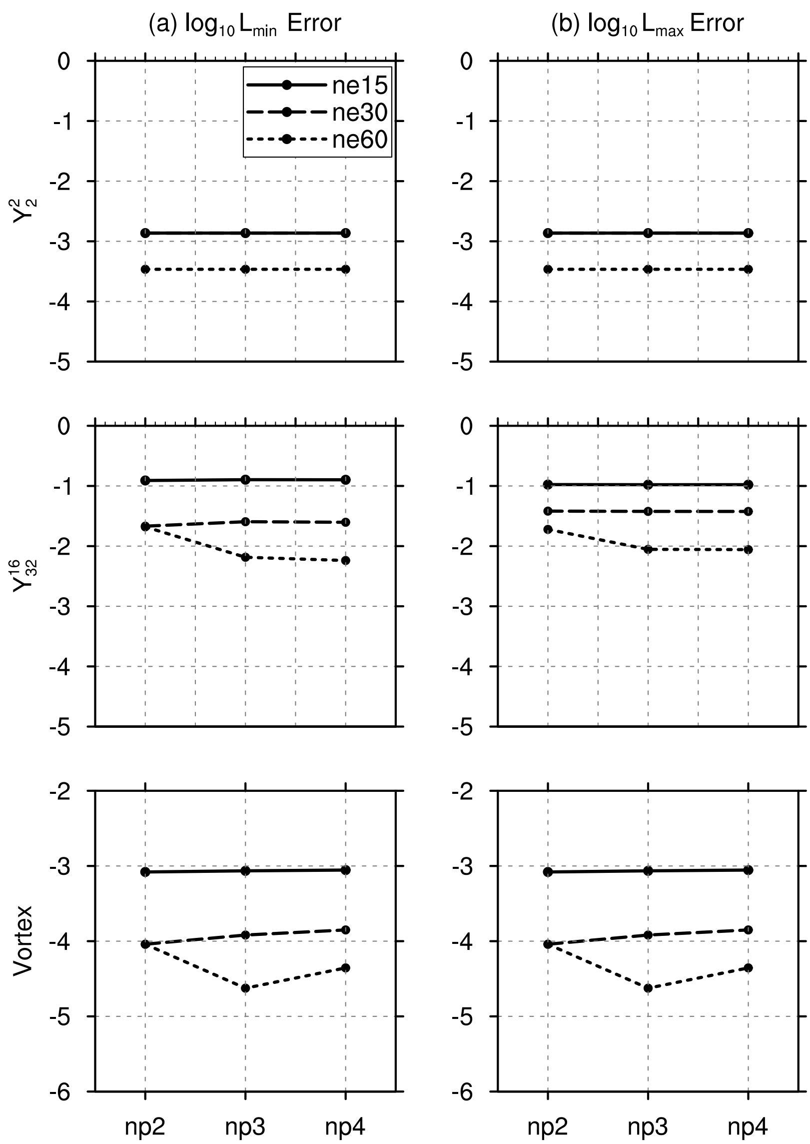

FIG. 8: Absolute L_{min} and L_{max} error norms reported for conservative and consistent remapping of the three idealized fields from the finite-volume cubed-sphere mesh to the tessellated $n_e = 30$ cubed-sphere mesh for source mesh cubed-sphere resolutions $n_e = 15, 30, 60$, rectangular truncation and for four orders of accuracy $N_p^t = 2, 3, 4$ on the target mesh. Undershoots (left) and overshoots (right) are indicated by circled data points.

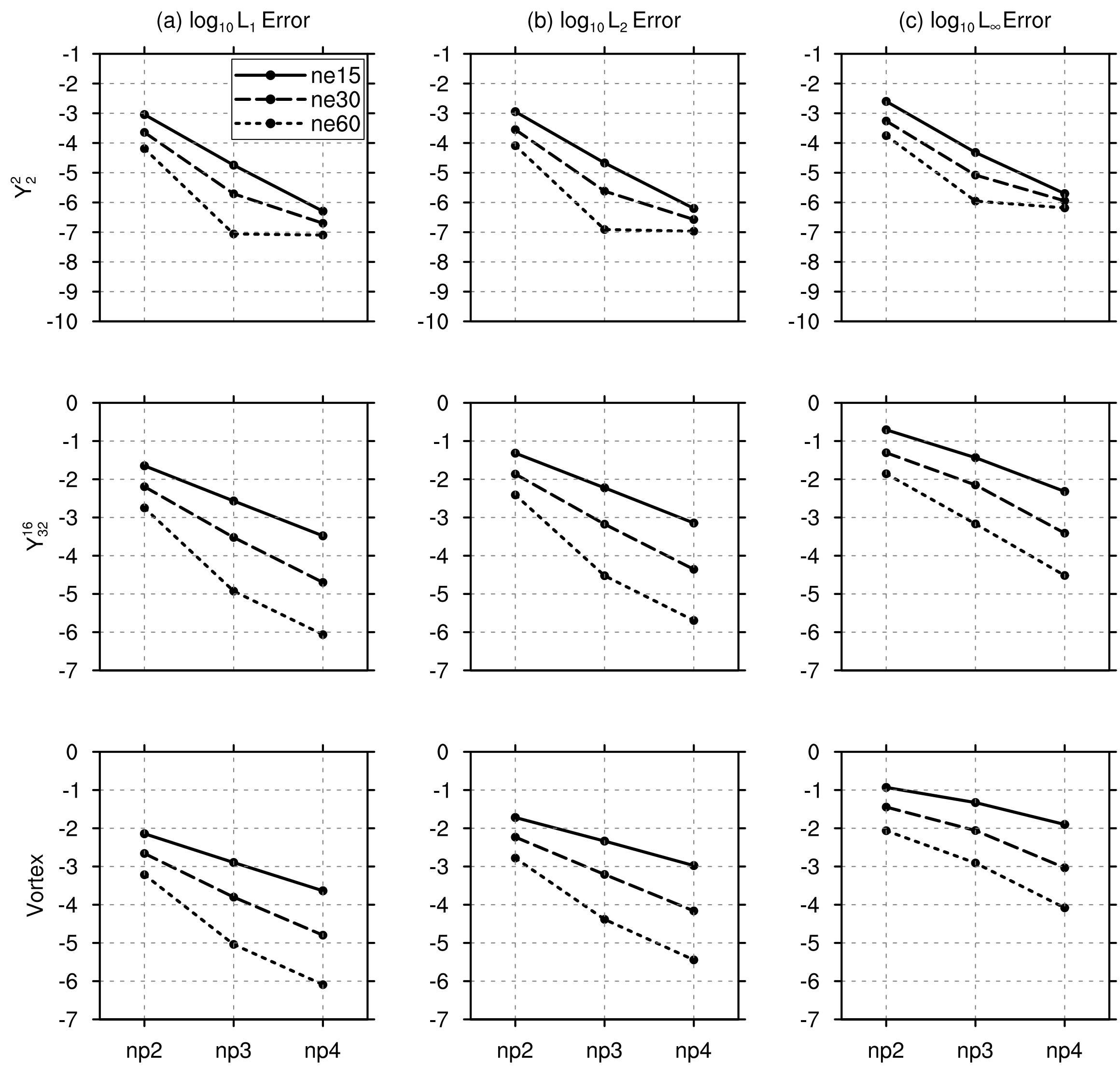

FIG. 9: Standard L_1, L_2 and L_∞ error norms reported for conservative and consistent remapping of the three idealized fields from the cubed-sphere mesh to the $n_i = 16$ icosahedral flag grid for cubed-sphere resolutions $n_e = 15, 30, 60$ and for three orders of accuracy $N_p^s = N_p^t = 2, 3, 4$.

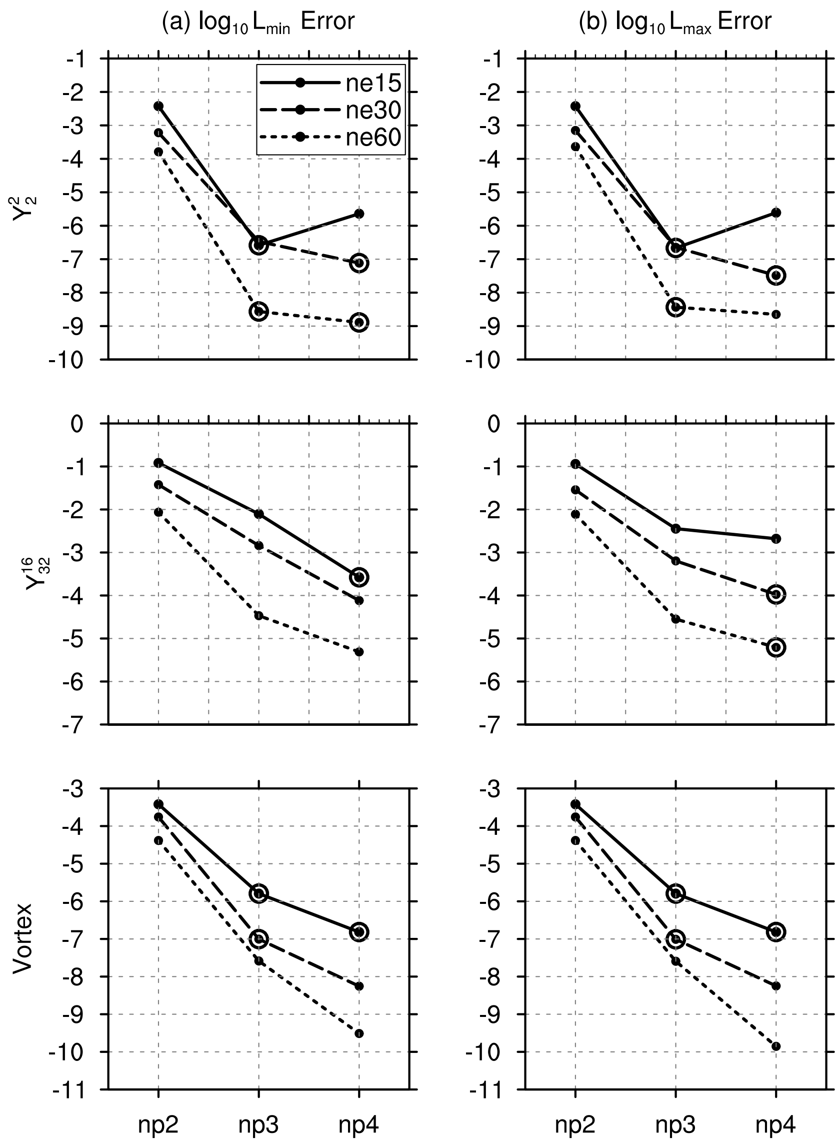

FIG. 10: Absolute L_{min} and L_{max} error norms reported for conservative and consistent remapping of the three idealized fields from the cubed-sphere mesh to the $n_i = 16$ icosahedral flag grid for cubed-sphere resolutions $n_e = 15, 30, 60$ and for three orders of accuracy $N_p^s = N_p^t = 2, 3, 4$. Undershoots (left) and overshoots (right) are indicated by circled data points.